Manipulating Impulsive Stimulated Raman Spectroscopy with a Chirped Probe Pulse

Lorenzo Monacelli,[†] Giovanni Batignani,[†,‡] Giuseppe Fumero,[†,§] Carino Ferrante,[†] Shaul Mukamel,[∥] and Tullio Scopigno[*,†,⊥]

[†]Dipartimento di Fisica, Universitá di Roma "La Sapienza", Roma I-00185, Italy

[‡]Dipartimento di Scienze Fisiche e Chimiche, Universitá degli Studi dell'Aquila, L'Aquila I-67100, Italy

[§]Dipartimento di Scienze di Base e Applicate per l'Ingegneria, Universitá di Roma "La Sapienza", Roma I-00185, Italy

[∥]Department of Chemistry, University of California, Irvine, California 92697-2025, United States

[⊥]Istituto Italiano di Tecnologia, Center for Life Nano Science @Sapienza, Roma I-00161, Italy

S *Supporting Information*

ABSTRACT: Photophysical and photochemical processes are often dominated by molecular vibrations in various electronic states. Dissecting the corresponding, often overlapping, spectroscopic signals from different electronic states is a challenge hampering their interpretation. Here we address impulsive stimulated Raman spectroscopy (ISRS), a powerful technique able to coherently stimulate and record Raman-active modes using broadband pulses. Using a quantum-mechanical treatment of the ISRS process, we show the mode-specific way the various spectral components of the broadband probe contribute to the signal generated at a given wavelength. We experimentally demonstrate how to manipulate the signal by varying the probe chirp and the phase-matching across the sample, thereby affecting the relative phase between the various contributions to the signal. These novel control knobs allow us to selectively enhance desired vibrational features and distinguish spectral components arising from different excited states.
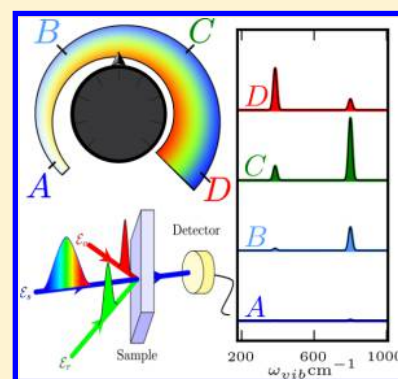
Ultrafast spectroscopy aims to study nonequilibrium atomic and molecular dynamics in the gas phase or the condensed phase on the femtosecond time scale.[1] This is most simply achieved by the pump−probe technique: an actinic pump beam prepares the sample in a nonstationary superposition state, while the transmission of a delayed probe subsequently reveals the state of the system at a given instant following photoexcitation. Ultrafast spectroscopy has witnessed a significant growth during the last two decades thanks to the development of temporal compression techniques, able to synthesize optical pulses with a few femtosecond duration and Fourier-transform-limited bandwidth.[2] This is a key tool for several spectroscopic approaches based on multiple pulses sequences, such as impulsive stimulated Raman spectroscopy (ISRS).[3−5]

The ISRS experiment exploits a time-domain *probe* protocol consisting of two temporally separated laser fields, the Raman and the probe pulses, to stimulate and read out vibrational coherences on a given electronic state, respectively. Consequently, it is not hampered by the background signals induced by the temporal overlap of multiple pulses, commonly affecting other kinds of ultrafast experiments.[6,7] The ISRS signal records the changes in the transmitted probe pulse as a function of its temporal delay with respect to the Raman pulse, T, and its wavelength λ_s, thereby resulting in a 2D signal. Fourier transforming over T recovers the spontaneous Raman spectrum. The heterodyne detection of ISRS spectra, engraved onto the highly directional probe field, suppresses fluorescence and other incoherent processes. The addition of a photochemical actinic *pump* allows for mapping out vibrational dynamics, triggering the system photoreaction with high temporal resolution.[8]

The power of ISRS has been recently demonstrated by investigating prototypical cases of photoinduced dynamics in Bacteriorhodopsin,[9] intermolecular vibrational motions in liquid CS_2,[10] isomerization of Channelrhodopsins,[11] and the excited-state proton transfer of green fluorescent protein.[12] The ISRS probing process is, in general, affected by concurring vibrational coherences from both the ground and excited states, and discerning the two is a most challenging task. Much effort has been made in this direction.[6] Strategies to identify the electronic state hosting a vibrational coherence at its generation have been proposed based on temporal dispersion by introducing a chirped resonant pump pulse.[13−15] Furthermore, ISRS extension to study the presence of electronic coherences in the X-ray domain[16,17] has been theoretically demonstrated.
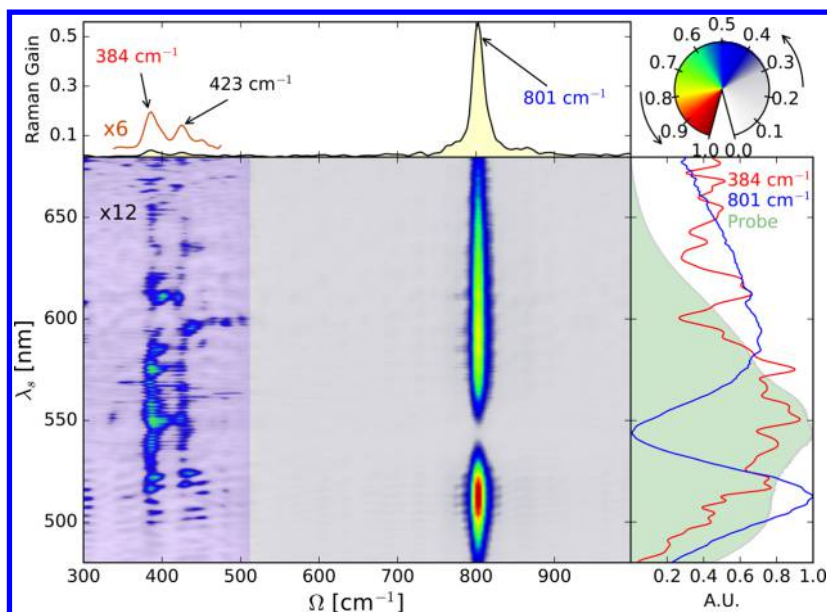
Figure 1. 2D broadband ISRS spectrum of cyclohexane as a function of the probe wavelength and the Raman frequency. The intensity of the 800 cm^{-1} mode exhibits a minimum in correspondence of the maximum probe intensity (reported in the right panel as green shaded area), with two maxima on the red and the blue sides of the probe central wavelength. The 384 cm^{-1} mode shows an opposite behavior, with the maximum in the center position. The top panel shows the marginal spectrum obtained by integrating over all probe wavelengths. The amplitude of the 384 and 800 cm^{-1} modes as a function of the probe wavelength is reported in the right panel (red and blue lines, respectively).

Here we study a three-beam experimental ISRS configuration. We start by a photoexcitation using a resonant actinic pulse (AP), followed by an ISRS detection, which combines an off-resonant Raman pulse (RP) and, critically, a properly shaped, chirped, broadband white-light continuum (WLC) probe. This allows us to unveil the undetermined population states following the photoreaction process triggered by the AP. Keeping the Raman pulse electronically off-resonant guarantees that the vibrational coherence is solely generated in the electronic state manifold involved in the photoreaction process, preventing contributions arising from additional electronic resonances. Moreover, taking advantage of a chirped WLC probe pulse provides access to the higher frequency region of the Raman spectrum (compared with a noncollinear optical parametric amplifier-based probe) without compromising the temporal resolution.[18] Last, but not least, introducing nonresonant chirped WLC, we demonstrate mode-selective enhancement of the ISRS signal.

We theoretically describe ISRS signals and their variation with the scattering geometry, elucidating the role of the phase-matching condition and the effect of a strongly chirped probe pulse. The response of the system is derived using a perturbative framework based on the diagrammatic expansion of the density matrix,[19,20] which allows us to take into account individually all of the nonlinear processes underlying the ISRS signal. Finally, we demonstrate how chirping and phase matching can be used to disentangle ground state from excited-state vibrational coherences.

The interpretation of broadband ISRS spectra is not easy, even in the apparently simple case of nonresonant probe pulses and in the absence of AP excitation reported in Figure 1. Here we show a broadband ISRS experiment, performed in a common solvent, liquid cyclohexane (C_6H_{12}). The ISRS signal intensity as a function of the probe wavelength, measured with an off-resonant Raman pulse, clearly reveals a different behavior of various vibrational ground-state modes.

The 384 cm^{-1} mode has the maximum of its intensity around the center of the probe λ_s = 555 nm, while the 800 cm^{-1} mode shows a minimum in the same wavelength region. The behavior of the 800 cm^{-1} mode is well described by previous theoretical descriptions based on classical or semiclassical approaches,[5,21,22] which predict a bilobed profile in the probe-wavelength resolved 2D maps across each vibrational mode. In the time domain, this corresponds to an amplitude modulation of the probe pulse at the stimulated vibrational frequencies, which vanishes at the spectral maximum. Notably, the red and blue spectral wings oscillate with an opposite phase. However, the 384 cm^{-1} mode signal in Figure 1 behaves differently, suggesting a more complex underlying process. To understand these differences, we derive the ISRS spectral response, taking into account probe chirp and finite sample size effects, within a quantum perturbation theory framework.

In the dipole approximation,[23] the ISRS process is described by the dipole Power−Zienau[24] radiation−matter interaction Hamiltonian $H_I = \vec{\mu}\cdot\vec{E}$, where $\vec{\mu}$ and $\vec{E}$ are the dipole and the local electric field operators. $\vec{E}$ can be separated into creation and annihilation operators

$$\vec{E} = \sum_{j,\alpha} \hat{e}_\alpha[\mathcal{E}_j(\vec{r}, t) + \mathcal{E}_j^\dagger(\vec{r}, t)] \tag{1}$$

where $\hat{e}_\alpha$ and j run over the polarization and mode of the fields, respectively. The ISRS heterodyne-detected signal can be defined as the derivative of the mean number of photons N_s in mode s of the probe pulse[25,26]

$$S = \int_{-\infty}^{+\infty} \frac{d\langle N_s \rangle}{dt'} \, dt' = \frac{i}{\hbar}\langle (V + V^\dagger)(\mathcal{E}_s - \mathcal{E}_s^\dagger) \rangle \tag{2}$$

where V and $V^\dagger$ represent the molecule excitation lowering and raising operators (see Methods).

We consider here the ISRS pulse sequence shown in Figure 2a. The actinic pulse promotes the system into an electronic
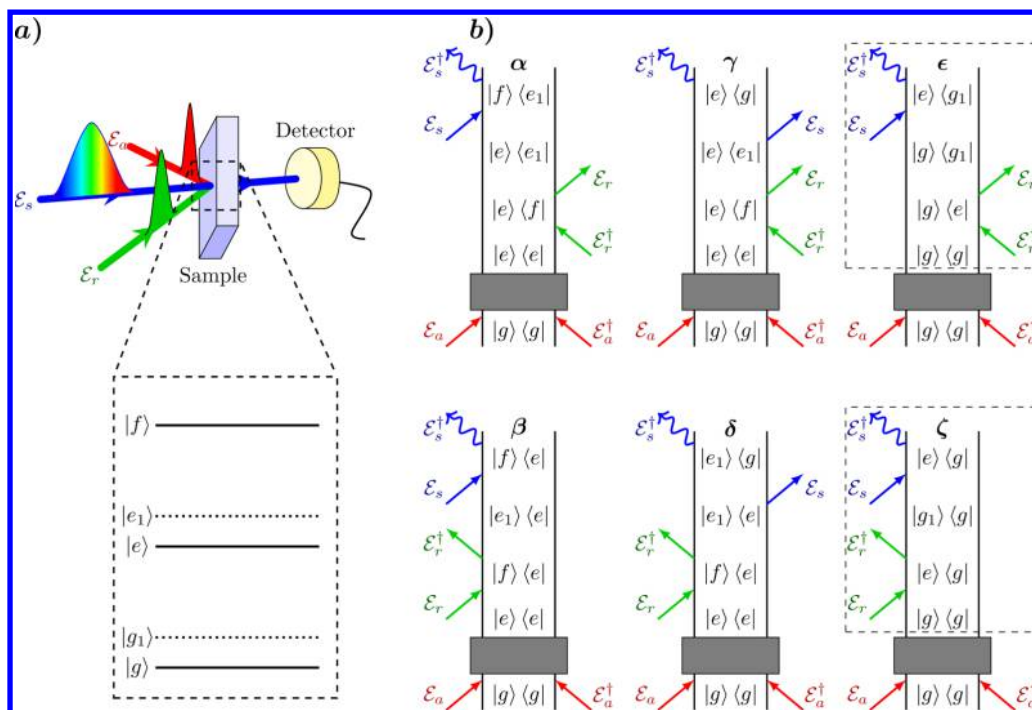
967

Figure 2. (a) ISRS experiment geometry and temporal envelopes of the laser fields are represented. Energy ladder scheme involved in the ISRS optical transitions is also indicated. We consider three electronic states g (ground), e, and f (excited); g_1 and e_1 are the corresponding vibrationally excited states. (b) Feynman diagrams for the ISRS process. Upon resonant actinic pump excitation, the system may evolve, ending up in an unknown population state (either the ground g or the electronically excited e) depending on the specific relaxation pathway (gray boxes). Dashed boxes represent the two ISRS signals surviving in the absence of actinic photoexcitation.

excited state, which can only relax (before the Raman pulse arrival time) down to the ground g or to the electronically excited state e, depending on its relaxation dynamics (indicated by the gray boxes in Figure 2b). At this point, the system could be vibrationally excited, as it happens in the presence of hot vibrational populations[27,28] or time-dependent frequencies along reaction coordinates.[29,30] However, for the sake of simplicity, we will consider in the following vibrationally relaxed cases. Accordingly, we will not include the actinic excitation pulse explicitly in the calculation, rather considering a molecular system characterized by three

electronic levels g, e, and f and a single (common) vibrational mode (see Figure 2a). In this case, the ISRS signal is described by the six $\alpha-\zeta$ diagrams in Figure 2b. The above possible extensions can be handled by evaluating additional diagrams originating from hot electronic states, weighted by the instantaneous thermal population, or by accounting for delay-dependent Green functions in eq 3.

Using the Heisenberg equation to calculate the derivative in eq 2,[20,31] the ISRS signal can be read out from the diagrams in Figure 2b

$$
\begin{aligned}
S(T, \omega_s) = \frac{2\mu_{ef}^2\mu_{e_1f}^2}{\hbar^4}\Im\Bigg\{ & \int_{-\infty}^{\infty}\int_{-\infty}^{\infty}\int_{-\infty}^{\infty} d\omega_1\, d\omega_2\, d\omega_3\, \tilde{E}_r^*(\omega_1, T)\tilde{E}_r(\omega_2, T)\tilde{E}_s(\omega_3)\tilde{E}_s^*(\omega_s)\delta(\omega_s - \omega_3 + \omega_2 - \omega_1) \\[4pt]
& \Big[\mathrm{Tr}\Big(V G_{fe_1}(\omega_3 + \omega_2 - \omega_1)V^\dagger G_{ee_1}(\omega_2 - \omega_1)V^\dagger G_{ef}(-\omega_1)V\rho_{ee}\Big) \\[4pt]
& + \mathrm{Tr}\Big(V G_{fe}(\omega_3 - \omega_2 + \omega_1)V^\dagger G_{e_1e}(\omega_1 - \omega_2)V G_{fe}(\omega_1)V^\dagger \rho_{ee}\Big) \\[4pt]
& - \mathrm{Tr}\Big(V G_{eg}(\omega_3 + \omega_2 - \omega_1)V^\dagger G_{ee_1}(\omega_2 - \omega_1)V^\dagger G_{ef}(-\omega_1)V\rho_{ee}\Big) \\[4pt]
& - \mathrm{Tr}\Big(V G_{e_1g}(\omega_3 - \omega_2 + \omega_1)V^\dagger G_{e_1e}(\omega_1 - \omega_2)V G_{fe}(\omega_1)V^\dagger \rho_{ee}\Big) \\[4pt]
& + \mathrm{Tr}\Big(V G_{eg_1}(\omega_3 + \omega_2 - \omega_1)V^\dagger G_{gg_1}(\omega_2 - \omega_1)V^\dagger G_{ge}(-\omega_1)V\rho_{gg}\Big) \\[4pt]
& + \mathrm{Tr}\Big(V G_{eg}(\omega_3 - \omega_2 + \omega_1)V^\dagger G_{g_1g}(\omega_1 - \omega_2)V G_{eg}(\omega_1)V^\dagger \rho_{gg}\Big) \Big]\Bigg\}
\end{aligned}
$$

$$(3)$$

where $G_{ij}(\omega) = (\omega - \omega_{ij} + i\eta)^{-1}$ is the matrix element of the frequency domain Green's function, η a positive infinitesimal
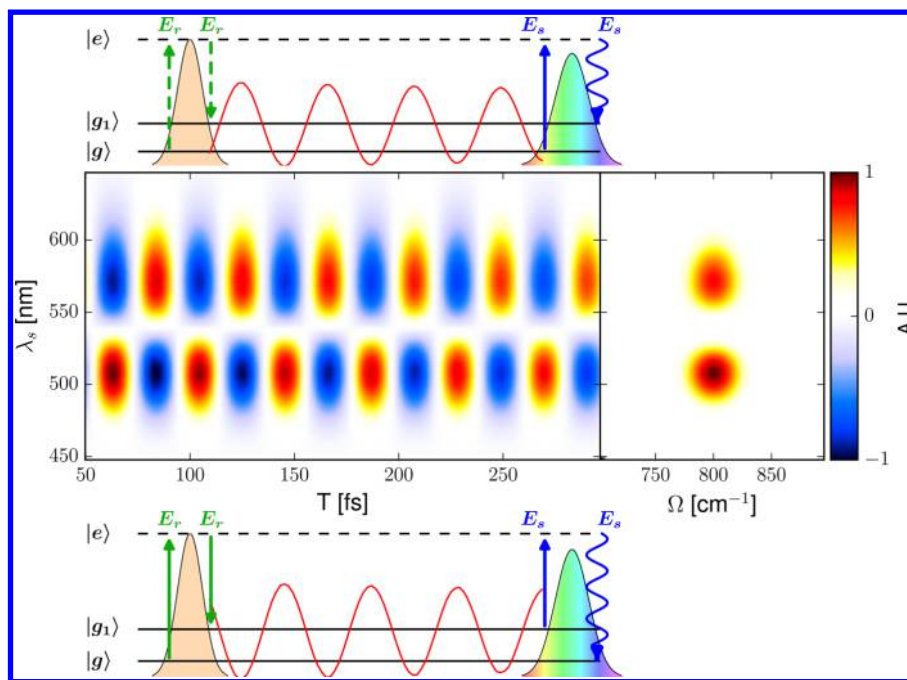
Figure 3. Simulation of the nonresonant third-order ISRS response (eq 4) for $\Delta k(\omega_1, \omega_2) = 0$ in the absence of actinic photoexcitation. Central panel: 2D map of $S(T, \lambda_s)$ and $S(\Omega, \lambda_s)$. The two energy ladder diagrams that describe the process, corresponding to the boxed section of the $\epsilon-\zeta$ Feynman diagrams in Figure 2b, are shown. The signal arises from the interference of these two pathways that generate time oscillations with opposite phases and cancel out in the central region of the spectrum, resulting in a bilobed profile along λ_s for each vibrational mode.

that ensures causality, and ρ_{ee} (ρ_{gg}) is the density matrix in the excited (ground) electronic state at the Raman pulse arrival time after the preparation process.

Calculating the matter correlation functions, taking into account for the finite sample length in a pencil shaped sample aligned with the probe pulse direction, as shown in the Methods section, eq 3 is recast as

$$S(T, \omega_s) = \frac{2\mu_{ef}^2 \mu_{e'f}^2}{\hbar^4} \Im \left\{ \sum_{j=\alpha-\zeta} \int_{-\infty}^{\infty} d\omega_1 \, d\omega_2 \right.$$

$$\tilde{E}_r^*(\omega_1, T)\tilde{E}_r(\omega_2, T)\tilde{E}_s(\omega_s + \omega_1 - \omega_2)\tilde{E}_s^*(\omega_s)$$

$$\text{sinc}\left[\frac{\vec{\Delta k}(\omega_1, \omega_2)\cdot\hat{z}L}{2}\right] \exp\left(i\frac{\vec{\Delta k}(\omega_1, \omega_2)}{2}\cdot\hat{z}L\right)$$

$$\left. P_j(-T)F_j(\omega_s, \omega_1, \omega_2) \right\} \tag{4}$$

where ω_s is the detected probe frequency, $\Im(z)$ indicates the imaginary part of z, $\tilde{E}_i$ stands for the spectral envelope of the i pulse, and $\tilde{\omega}_{ij} = \omega_i - \omega_j - i\gamma_{ij}$, where γ_{ij} is the dephasing rate of the vibrational coherence between i and j. $P_j(-T)$ indicates the population in the excited electronic state for diagrams $j = \alpha - \delta$ and in the ground state for diagrams $j = \epsilon - \zeta$ at the arrival time $(-T)$ of the Raman pulse. The correlation functions $F_j(\omega_s, \omega_1, \omega_2)$ contain the matter response, and $\Delta k(\omega_1, \omega_2)$ indicates the phase-matching condition for the six diagrams. Both are given in the Methods section, as well as the details of eq 4 derivation.[25]

We define the 2D signal $S(\Omega, \omega_s)$ as

$$S(\Omega, \omega_s) = \int_{-\infty}^{\infty} dT \, e^{i\Omega T} S(T, \omega_s) \tag{5}$$

In the following, we show experimental and simulated signals as a function of the wavelength $\lambda_s = \frac{2\pi}{\omega_s}$, instead of the angular frequency ω_s, to be consistent with the previous literature.[12,32]

To interpret the experimental results reported in Figure 1, eq 3 needs to be evaluated without the effect of the actinic photoexcitation and for off-resonant Raman and probe pulses. This is done by retaining the last two terms corresponding to the third-order processes indicated in the dashed boxes of the $\epsilon-\zeta$ diagrams in Figure 2b. Because the pulses wavelengths are far from any electronic transition, the rotating wave approximation (RWA) cannot be made and, in principle, six additional diagrams should be taken into account. However, as shown in the Supporting Information, they generate signals that are identical to those from ϵ and ζ diagrams.

At first, we neglect the dispersion in the sample and the chirp on the probe pulse and consider a collinear pulse geometry. Thus setting $\Delta k = 0$ in eq 4, we obtain the 2D signal shown in Figure 3. The two contributions oscillate with an opposite phase, in agreement with predictions of previous models.[22]

More generally, because of the finite sample length, the phase-matching condition can significantly influence the signal due to wave vector dispersion. For $\Delta k \neq 0$, it is possible to integrate eq 4 analytically for Lorentzian pulse envelopes (see the Supporting Information). This offers a test for the numerical integration in the case of general envelopes. A numerical integration of eq 5, performed using transform limited Gaussian envelopes, with $\lambda_{WLC} = 540$ nm, $\Delta\lambda_{WLC} = 100$ nm, $\lambda_{RP} = 545$ nm, and $\Delta\lambda_{RP} = 60$ nm in a noncollinear geometry (with an angle $\theta = 4°$ between the Raman pulse and the WLC), is reported Figure 4a,b.
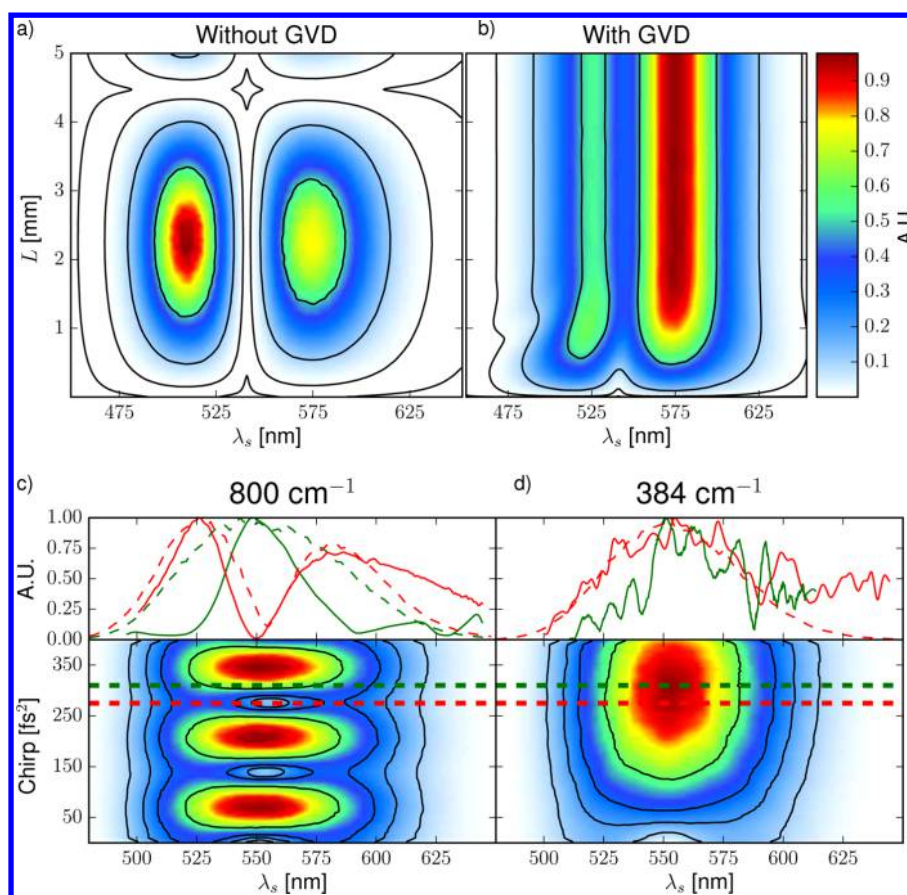
Figure 4. $S(\Omega = 800\ \text{cm}^{-1}, \lambda_s)$, from eq 5, as a function of the sample length L and the probe chirp, for nonresonant ISRS in absence of actinic photoexcitation. In panel a, the sample is considered as a nondispersive medium (all spectral components propagate with the same velocity), and the phase-matching condition is ruled only by the relative angle between the Raman and probe pulses ($\theta = 4°$). Under this regime, the phase mismatch produces a wavelength-independent phase factor, periodically modulating the signal in L. In panel b, the dispersion curve of cyclohexane has been taken into account. While propagating in the sample, the Raman pulse undergoes a temporal broadening due to the group velocity dispersion; this reflects in a critical length beyond which the Raman pulse is longer than the vibrational mode period and the signal is no more generated, breaking the periodicity over L. Panels c and d depict the signal dependence on the probe chirp for two different vibrational modes. The experimental data (dashed lines in the plots) are overlapped with the theoretical simulations (solid lines) for two different values of the probe chirp, indicated by the dashed horizontal lines in the colormaps. The red features correspond to those presented in Figure 1.

In Figure 4a, we assume a nondispersive medium, with a dispersion curve $n(\lambda)$ constant over all wavelengths. The $\Delta k(\omega_1, \omega_2)$ term in eq 4 carries a wavelength-independent phase factor, which modulates the ISRS intensity over L but does not affect the spectral shape of the signal. In Figure 4b, the experimental dispersion curve of the cyclohexane[33] has been used to calculate the $\Delta k(\omega_1, \omega_2)$ function in eq 21. In this case, the spectral shape of the signal is affected by the group velocity dispersion (GVD), which acts asymmetrically for the two pathways ϵ and ζ that generate the signal. Because the phase mismatch is different for the two diagrams, they yield different amplitudes, resulting in the asymmetric double peak profile in Figure 4b. The presence of a phase factor between the two interfering diagrams also prevents a total cancellation of the ISRS signal around the central wavelength of the probe.

The GVD further induces a temporal broadening of the Raman and probe pulses, while propagating along the sample. When the duration of the Raman pulse is longer than the vibrational mode period ($T_{e_1 e} = \frac{2\pi}{\omega_{e_1 e}}$) the signal cannot be coherently generated. Hence, for sample size greater than a critical length (L_c, usually few millimeters), the signal reaches a stationary intensity. L_c depends on the Raman pulse initial duration, on the beam relative angle, on the vibrational mode frequency and on the sample group velocity dispersion. Notably, the suppression of the ISRS signal for $L > L_c$, as soon as the Raman pulse is temporal profile is stretched to a duration longer than $T_{e_1 e}$, also sets an upper limit for the temporal resolution in ISRS-based pump–probe experiments. This is a useful advantage over other kinds of ultrafast measurements, where the temporal broadening of the pulses diminishes the temporal resolution.

Our results may be used to rationalize the experimental results reported by Kukura et. al,[3] who reported the ISRS spectral dependence on the sample size. They had pointed out that the intensity normalized by the number of molecules decreases as the sample length increases as a result of the combination between GVD and group velocity mismatch (GVM) between the Raman and the probe pulse. The intensity decrease with L can be also explained in the absence of these two phenomena (Figure 4a): the signal varies with the length of the sample in a sinusoidal fashion, while the number of molecules grows linearly. This would imply signal attenuation independent of the wavelength. Instead, Kukura et al. observed that the signal blue side is suppressed strongly:
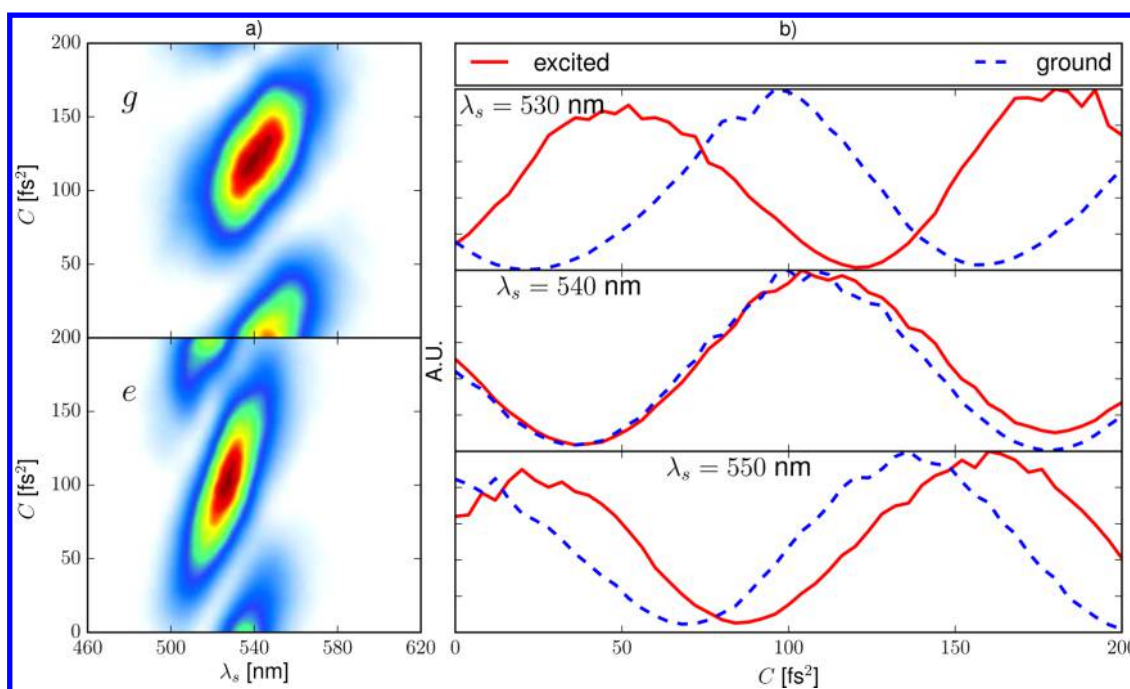
Figure 5. (a) $S(\Omega = 800 \text{ cm}^{-1}, \lambda_s, C)$ ISRS signal intensity from eqs 5 and 6 for a 800 cm^{-1} vibrational mode as a function of the probed wavelength and the probe chirp, C, for the processes starting from the ground state $|g\rangle\langle g|$ (top panel and $\epsilon-\zeta$ diagrams) and the excited state $|e\rangle\langle e|$ (bottom panel and $\alpha-\beta-\gamma-\delta$ diagrams). The probe is tuned in resonance with all electronic transitions involved in the six diagrams. The shape of the signal is stretched along the chirp direction for vibrational coherences generated in the electronic excited state due to the destructive interference between $\alpha-\gamma$ and $\beta-\delta$ pathways. (b) Signal intensity as a function of C at selected probe wavelengths. The wavelength-dependent phase of Raman mode amplitude enables us to distinguish between the electronic levels in which the vibrational coherence is generated.

this can be explained as an effect of GVD that suppresses the blue-side peak (Figure 4b).

Remarkably, while the sample geometry and the GVD can significantly modulate the signal shape, because the two diagrams interfere destructively, they cannot generate single-lobe profiles centered around the maximum of the probe, such as reported in Figure 1.

The effect of a linear chirp of the probe can be taken into account in eq 4 by introducing a chirp (C) dependence in the probe electric field envelope

$$\tilde{E}_s(\omega, C) = \tilde{E}_s(\omega)e^{iC(\omega-\omega_0)^2} \qquad (6)$$

where the leading frequency is indicated as ω_0 and $\tilde{E}_s(\omega) = \frac{1}{\sigma_s\sqrt{2\pi}}e^{-(\omega-\omega_0)^2/2\sigma_s^2}$ is the Gaussian envelope of the electric probe field (centered in ω_0).

As shown in Figure 4c,d, chirping the probe pulse strongly affects the spectral shape of the signal because it modifies the relative phase between the two Feynman diagrams ϵ and ζ. The 2D maps report the intensity of the 800 and 384 cm^{-1} modes of cyclohexane as a function of C and λ_s. On the top of Figure 4c,d, the experimental results (continuous lines) for two different chirped probe pulses are compared with the simulations (dashed lines), showing a good agreement. Modifying the chirp enables us to reshape and enhance the signal profile, in particular, switching from a bilobed to a monolobed dependence over the probe wavelength, as shown for the 800 cm^{-1} mode (red and green lines in of Figure 4c). This peculiar behavior can be easily interpreted. The ISRS signal is generated by the linear superposition of two Liouville pathways, represented by the Feynman diagrams ϵ and ζ in Figure 2b. Each diagram involves a different frequency component of the probe, which is shifted (with respect to the probed one) by the vibrational mode revealed by the signal. Consequently, on the tails of the probe spectrum, only one diagram dominates, the one generated by a frequency in which the probe is more intense. At the center of the probe spectrum, the two diagrams are in counter-phase and they cancel out. However, chirping the probe introduces a phase difference between the two contributions generating the signal. This means that there are some periodic values of the chirp in which the two diagrams constructively interfere, leading to a strong signal enhancement. Because the relative phase between the processes generating the ISRS response introduced by the WLC chirp depends quadratically on the observed vibrational frequency, the 384 cm^{-1} mode is much more weakly dependent on the probe chirp than the 800 cm^{-1}, as shown in Figure 4b,c. A small WLC chirp (50 fs^2) causes a relative phase between diagram $\epsilon-\zeta$ for the 384 cm^{-1} Raman mode, making the two components no longer opposite in phase and turning the bilobed shape into a (much more intense) monolobed one. This behavior survives even for much higher values of chirp (>400 fs^2), resulting in a monolobed profile for all explored chirp values. Only a higher value of C ($\sim$500 fs^2) would generate the bilobed profile, with destructive interference between ϵ and ζ.

Introducing a chirp on the probe pulse can be used to enhance specific vibrational modes and, most importantly, to separate contributions involving different potential energy surfaces upon resonant actinic excitation. Under such circumstances, the contributions from the two additional diagrams $\alpha-\beta$ in Figure 2b should be included in the ISRS response. Notably, the corresponding additional signals are identical to diagrams $\epsilon-\zeta$ and therefore do not allow us to discriminate between processes involving ground or excited states. This goal can be achieved by a resonant probe, which

has two consequences: (i) the signals corresponding to $\alpha-\beta$ and $\epsilon-\zeta$ are no longer the same and (ii) two additional diagrams ($\gamma-\delta$) arise.

We now apply the proposed chirped probe scheme to the more challenging case of overlapping electronic resonances, where the resonance condition occurs in the same probe wavelength region, and hence the broadband nature of the probe could not be directly exploited to discriminate the involved electronic transition. The vibrational and electronic energy levels considered are shown in the diagram of Figure 2a, together with the pulse scheme used in the proposed experiment. In Figure 5, we show the corresponding ISRS response for a 800 cm^{-1} Raman mode, reproducing the vibrational peak amplitude as a function of the probe chirp C and wavelength λ_s. In the top panel of Figure 5a, only diagrams $\epsilon-\zeta$ for a system prepared in the electronic ground state are switched on, while in the bottom panel, the 2D signal is calculated for diagrams $\alpha-\delta$, where only the states prepared in the excited electronic state $|e\rangle\langle e|$ are interrogated by the ISRS process. As emphasized by the slices for fixed probed wavelength shown in Figure 5b, the specific involved electronic resonance introduces a wavelength-dependent phase shift on the chirp axis between the ISRS signal generated by a system prepared in the ground state and one in the excited state, as can be seen in eqs 15−20. Such a resonance-specific phase-factor can be conveniently sampled, taking advantage of the broadband nature of the probe pulse, which ensures us to access spectral regions strongly sensitive to the involved electronic level. This establishes a novel method to assign vibrational features to specific electronic states.

In summary, we have investigated the role of phase matching and probe chirp conditions in an ISRS experiment, through a diagrammatic treatment of the signal generation, enabling us to dissect the pathways that generate the nonlinear response and to rationalize the spectral dependence on the probe wavelength.

The ISRS signal, for a given detected wavelength, indeed results from the sum of concurring and distinct third-order processes, associated with photons, which are red- and blue-shifted by one vibrational quantum. This gives rise to contributions oscillating as a function of the time delay between the Raman and probe pulses.

In off-resonant ISRS with unchirped pulse, the two oscillations interfere destructively, explaining the strong signal suppression that can be observed in the central part of the spectrum. This explains why the weak Raman bands are often buried in the noise.

Our results suggest that an optimal probe chirping profile can be used to selectively enhance specific vibrational modes and are relevant for signal analysis improvement. The identification of the signal dependence on the probe wavelength for each mode indeed allows us to perform the correct weighted average over the entire probe spectrum, improving the signal-to-noise ratio.

Furthermore, our results establish a way to assign a given vibrational dynamics to the relevant potential energy surface: fine-tuning the relative phase between the processes contributing to the signal generation represents a powerful control knob to assign spectral features to specific electronic states, allowing for discerning excited from ground-state vibrational coherences.

■ METHODS

The $\vec{\mu}$ and $\vec{E}$ terms in the interaction Hamiltonian indicate the dipole and the local electric field operators and can be expressed as

$$\vec{\mu} = \sum_{i,j,i\neq j} \vec{\mu}_{ij}|i\rangle\langle j| \quad \vec{\mu}_{ij} = \langle i|e\sum_{\alpha} \vec{r}_{\alpha}|j\rangle \tag{7}$$

Here $|i\rangle$ indicates an eigenvector of the non interactive matter Hamiltonian and α is an index that runs over the atom positions.

The positive ($\mathcal{E}_j$) and negative ($\mathcal{E}_j^{\dagger}$) frequency components of the electric field can be expressed as

$$\mathcal{E}_j = \sqrt{\frac{\hbar\omega_j}{2\varepsilon_0 V}} a_j e^{-i(\omega_j t - \vec{k}_j \cdot \vec{r})} \quad \mathcal{E}_j^{\dagger} = \sqrt{\frac{\hbar\omega_j}{2\varepsilon_0 V}} a_j^{\dagger} e^{+i(\omega_j t - \vec{k}_j \cdot \vec{r})} \tag{8}$$

where j is the single mode of the electromagnetic radiation.

The time derivative of the number of photons in eq 2 has been computed using the Ehrenfest theorem,[20,31] and V is the molecular dipole transition operator

$$V = \sum_{i,j,j>i} \mu_{ij}|i\rangle\langle j| \qquad V + V^{\dagger} = \mu \tag{9}$$

We dropped the vectorial notation absorbing the thermodynamic average of the scalar product between the electric field polarization vector and the dipole in the symbol μ.

Considering an homogeneous 1D sample, the dipole operator is uniform

$$\mu(z) = \mu\theta(z)\theta(L - z) \tag{10}$$

where $\theta(z)$ is the Heaviside function. The coherent laser light state is an eigenvector of the electric field operator

$$\sum_j \mathcal{E}_j|E\rangle = E(t, \vec{r}, T)|E\rangle \tag{11}$$

Restricting along the z direction

$$E(t, \vec{r}, T) = \int_{-\infty}^{\infty} d\omega \, dk \, \tilde{E}(\omega, k, T) e^{-i\omega t + ikz\cos\vartheta} \tag{12}$$

Here ϑ is the angle between the chosen beam and the sample direction. The plane wave hypothesis leads to[19]

$$\tilde{E}(k, \omega, T) = \tilde{E}(\omega, T)\delta[k - k(\omega)] \tag{13}$$

where $k(\omega)$ contains the dispersion of the sample

$$k(\omega) = \frac{\omega}{c}n(\omega) \tag{14}$$

where n is the refractive index for the given frequency.

The density matrix formalism can be used to obtain the average in eq 2, through the relation $\langle O \rangle = \text{Tr}[O\rho(t)]$, which holds for a generic operator O; here the time evolution of the density matrix $\rho(t)$ can be evaluated by the perturbative expansion of the Liouville equation. The correlation functions $F_j(\omega_s,\omega_1,\omega_2)$ in eq 4 are given by

$$F_\alpha(\omega_s, \omega_1, \omega_2) = \frac{1}{(\omega_s - \tilde{\omega}_{fe_1})(\omega_1 + \tilde{\omega}_{ef})(\omega_1 - \omega_2 + \tilde{\omega}_{ee_1})} \tag{15}$$

$$F_\beta(\omega_s, \omega_1, \omega_2) = \frac{1}{(\omega_s - \tilde\omega_{fe})(\omega_2 - \tilde\omega_{fe})(\omega_2 - \omega_1 - \tilde\omega_{e_1 e})} \quad (16)$$

$$F_\gamma(\omega_s, \omega_1, \omega_2) = \frac{-1}{(\omega_s - \tilde\omega_{eg})(\omega_1 + \tilde\omega_{ef})(\omega_1 - \omega_2 + \tilde\omega_{ee_1})} \quad (17)$$

$$F_\delta(\omega_s, \omega_1, \omega_2) = \frac{-1}{(\omega_s - \tilde\omega_{e_1 g})(\omega_2 - \tilde\omega_{fe})(\omega_2 - \omega_1 - \tilde\omega_{e_1 e})} \quad (18)$$

$$F_\epsilon(\omega_s, \omega_1, \omega_2) = \frac{1}{(\omega_s - \tilde\omega_{eg_1})(\omega_1 + \tilde\omega_{ge})(\omega_1 - \omega_2 + \tilde\omega_{gg_1})} \quad (19)$$

$$F_\zeta(\omega_s, \omega_1, \omega_2) = \frac{1}{(\omega_s - \tilde\omega_{eg})(\omega_2 - \tilde\omega_{eg})(\omega_2 - \omega_1 - \tilde\omega_{g_1 g})} \quad (20)$$

and the $\Delta\vec{k}\,(\omega_1, \omega_2)$ phase mismatch is

$$\overrightarrow{\Delta k}(\omega_1, \omega_2) = -\vec{k}_a(\omega_1) + \vec{k}_a(\omega_2) + \vec{k}_s(\omega_s + \omega_1 - \omega_2) - \vec{k}_s(\omega_s) \quad (21)$$

The couples of eqs 15 and 16, 17 and 18, and 19 and 20 enlighten the fact that the resonance conditions for these diagrams, containing two distinct correlation functions, are different. In fact, considering, for example, eqs 15 and 16, the difference between ω_2 and ω_1 that maximizes the signal is, respectively, ω_{ee_1} and $\omega_{e_1 e}$. Remarkably, this leads to two different phase-matching condition in eq 21 for the two processes.

Moreover, the presence of different maximum conditions for these two diagrams ($\omega_1 - \omega_2 = \omega_{ee_1}$ and $\omega_2 - \omega_1 = \omega_{e_1 e} \to \omega_1 - \omega_2 = -\omega_{ee_1}$) rationalizes the π phase shift between the two pathways. In fact, in the off resonant regime, the imaginary parts of the denominator can be neglected, and hence the dominant contributions to the integrals in eq 4 are $\propto e^{i\omega_{ee1}T}$ and $\propto e^{-i\omega_{ee1}T}$, whose imaginary parts ($\sin[\omega_{ee_1}T]$ and $\sin[-\omega_{ee_1}T]$) oscillate with opposite phase.

Notably, when the probe wavelength is tuned to match the $e \to f$ electronic transition energy, the real part of the first denominators in eqs 15 and 16 cancels out, leaving an imaginary term proportional to the vibrational dephasing time. Hence, under resonant conditions, the leading contributions to the integral are $\propto i \cdot e^{i\omega_{ee1}T}$ and $\propto i \cdot e^{-i\omega_{ee1}T}$, whose imaginary parts ($\cos[\omega_{ee_1}T]$ and $\cos[-\omega_{ee_1}T]$) oscillate in phase. The analytic derivation of the phase relation between the Liouville pathways for Lorentzian pulse envelopes is reported in the Supporting Information.

The experimental setup exploited for the measurements on cyclohexane is based on a Ti:sapphire laser source that generates 3.6 mJ, 35 fs pulses at 800 nm and 1 kHz repetition rate. The Raman pulse is synthesized by a noncollinear optical parametric amplifier (NOPA) that produces tunable visible pulses in the range (500−700 nm) and compressed using chirped mirrors to ~10 fs. The time interval between the Raman and probe pulses is settled by a computer-controlled delay line on the Raman pulse optical path. The WLC probe pulse is synthesized, focusing part of the source pulse on a nonlinear medium plate. The shape of the spectral envelope can be varied by changing the parameters of super continuum generation inside the nonlinear crystal, such as the pump power and the material used for the WLC generation. The time duration of the Raman pulse is measured by second-harmonic noncollinear autocorrelation, while the probe chirp can be estimated from the relative delay of the onset of oscillations at different probe wavelengths. Notably, as shown in the Supporting Information, a more accurate characterization of the chirp can be extracted using as a reference the coherent artifact between the two beams

A synchronized chopper blocks alternating Raman pulses to record the modification induced to transmitted WLC probe, which is frequency-dispersed by a spectrometer onto a CCD device. The Raman spectrum is obtained from the detected oscillating temporal signal using fast Fourier transform (FFT) algorithm. Zero padding algorithm and specific spectral Kaiser−Bessel windowing are exploited to enhance the spectral definition.[3,34]

■ ASSOCIATED CONTENT

Ⓢ Supporting Information

The Supporting Information is available free of charge on the ACS Publications website at DOI: 10.1021/acs.jp-clett.6b03027.

> Derivation of signal analytic integration protocols for specific spectral profiles. Comments on the non-RWA diagrams. Details of chirp and phase measurements. (PDF)

■ AUTHOR INFORMATION

Corresponding Author

*E-mail: tullio.scopigno@phys.uniroma1.it.

ORCID ⓘ

Tullio Scopigno: 0000-0002-7437-4262

Notes

The authors declare no competing financial interest.

■ ACKNOWLEDGMENTS

■ REFERENCES

(1) Zewail, A. H. Femtochemistry: Atomic-Scale Dynamics of the Chemical Bond. *J. Phys. Chem. A* **2000**, *104*, 5660−5694.

(2) Manzoni, C.; Mücke, O. D.; Cirmi, G.; Fang, S.; Moses, J.; Huang, S.-W.; Hong, K.-H.; Cerullo, G.; Kärtner, F. X. Coherent Pulse Synthesis: Towards Sub-Cycle Optical Waveforms. *Laser Photon. Rev.* **2015**, *9*, 129−171.

(3) Liebel, M.; Schnedermann, C.; Wende, T.; Kukura, P. Principles and Applications of Broadband Impulsive Vibrational Spectroscopy. *J. Phys. Chem. A* **2015**, *119*, 9506−9517.

(4) Tanimura, Y.; Mukamel, S. Two-Dimensional Femtosecond Vibrational Spectroscopy of Liquids. *J. Chem. Phys.* **1993**, *99*, 9496−9511.

(5) Yan, Y.-X.; Gamble, E. B.; Nelson, K. A. Impulsive Stimulated Scattering: General Importance in Femtosecond Laser Pulse

Interactions with Matter, and Spectroscopic Applications. *J. Chem. Phys.* **1985**, *83*, 5391−5399.

(6) Liebel, M.; Kukura, P. Broad-Band Impulsive Vibrational Spectroscopy of Excited Electronic States in the Time Domain. *J. Phys. Chem. Lett.* **2013**, *4*, 1358−1364.

(7) Cheng, J.-X.; Xie, X. S. Coherent Anti-Stokes Raman Scattering Microscopy: Instrumentation, Theory, and Applications. *J. Phys. Chem. B* **2004**, *108*, 827−840.

(8) Tokmakoff, A.; Lang, M. J.; Larsen, D. S.; Fleming, G. R.; Chernyak, V.; Mukamel, S. Two-Dimensional Raman Spectroscopy of Vibrational Interactions in Liquids. *Phys. Rev. Lett.* **1997**, *79*, 2702−2705.

(9) Kahan, A.; Nahmias, O.; Friedman, N.; Sheves, M.; Ruhman, S. Following Photoinduced Dynamics in Bacteriorhodopsin with 7-fs Impulsive Vibrational Spectroscopy. *J. Am. Chem. Soc.* **2007**, *129*, 537−546.

(10) Ruhman, S.; Kohler, B.; Joly, A. G.; Nelson, K. A. Intermolecular Vibrational Motion in CS_2 Liquid at $165 \leqslant T \geqslant 300$ K Observed by Femtosecond Time-Resolved Impulsive Stimulated Scattering. *Chem. Phys. Lett.* **1987**, *141*, 16−24.

(11) Schnedermann, C.; Muders, V.; Ehrenberg, D.; Schlesinger, R.; Kukura, P.; Heberle, J. Vibronic Dynamics of the Ultrafast All-Trans to 13-Cis Photoisomerization of Retinal in Channelrhodopsin-1. *J. Am. Chem. Soc.* **2016**, *138*, 4757−4762.

(12) Fujisawa, T.; Kuramochi, H.; Hosoi, H.; Takeuchi, S.; Tahara, T. Role of Coherent Low-Frequency Motion in Excited-State Proton Transfer of Green Fluorescent Protein Studied by Time-Resolved Impulsive Stimulated Raman Spectroscopy. *J. Am. Chem. Soc.* **2016**, *138*, 3942−3945.

(13) Bardeen, C. J.; Wang, Q.; Shank, C. V. Selective Excitation of Vibrational Wave Packet Motion Using Chirped Pulses. *Phys. Rev. Lett.* **1995**, *75*, 3410−3413.

(14) Bardeen, C. J.; Wang, Q.; Shank, C. V. Femtosecond Chirped Pulse Excitation of Vibrational Wave Packets in LD690 and Bacteriorhodopsin. *J. Phys. Chem. A* **1998**, *102*, 2759−2766.

(15) Wand, A.; Kallush, S.; Shoshanim, O.; Bismuth, O.; Kosloff, R.; Ruhman, S. Chirp Effects on Impulsive Vibrational Spectroscopy: a Multimode Perspective. *Phys. Chem. Chem. Phys.* **2010**, *12*, 2149−2163.

(16) Biggs, J. D.; Zhang, Y.; Healion, D.; Mukamel, S. Multidimensional X-Ray Spectroscopy of Valence and Core Excitations in Cysteine. *J. Chem. Phys.* **2013**, *138*, 144303.

(17) Dorfman, K. E.; Bennett, K.; Mukamel, S. Detecting Electronic Coherence by Multidimensional Broadband Stimulated X-Ray Raman Signals. *Phys. Rev. A: At., Mol., Opt. Phys.* **2015**, *92*, 023826.

(18) Polli, D.; Brida, D.; Mukamel, S.; Lanzani, G.; Cerullo, G. Effective Temporal Resolution in Pump-Probe Spectroscopy with Strongly Chirped Pulses. *Phys. Rev. A: At., Mol., Opt. Phys.* **2010**, *82*, 053809.

(19) Mukamel, S. *Principles of Nonlinear Spectroscopy*; Oxford University Press, 1995.

(20) Rahav, S.; Mukamel, S. Ultrafast Nonlinear Optical Signals Viewed From the Molecule's Perspective: Kramers-Heisenberg Transition-Amplitudes Versus Susceptibilities. *Adv. At., Mol., Opt. Phys.* **2010**, *59*, 223−263.

(21) De Silvestri, S.; Fujimoto, J.; Ippen, E.; Gamble, E. B.; Williams, L. R.; Nelson, K. A. Femtosecond Time-Resolved Measurements of Optic Phonon Dephasing by Impulsive Stimulated Raman Scattering in α-Perylene Crystal From 20 to 300 K. *Chem. Phys. Lett.* **1985**, *116*, 146−152.

(22) Ruhman, S.; Joly, A.; Nelson, K. Coherent Molecular Vibrational Motion Observed in the Time Domain Through Impulsive Stimulated Raman Scattering. *IEEE J. Quantum Electron.* **1988**, *24*, 460−469.

(23) Babiker, M.; Loudon, R. Derivation of the Power-Zienau-Woolley Hamiltonian in Quantum Electrodynamics by Gauge Transformation. *Proc. R. Soc. London, Ser. A* **1983**, *385*, 439−460.

(24) Power, E. A.; Zienau, S. Coulomb Gauge in Non-Relativistic Quantum Electro-Dynamics and the Shape of Spectral Lines. *Philos. Trans. R. Soc., A* **1959**, *251*, 427−454.

(25) Dorfman, K. E.; Fingerhut, B. P.; Mukamel, S. Time-Resolved Broadband Raman Spectroscopies: a Unified Six-Wave-Mixing Representation. *J. Chem. Phys.* **2013**, *139*, 124113.

(26) Batignani, G.; Fumero, G.; Mukamel, S.; Scopigno, T. Energy Flow Between Spectral Components in 2D Broadband Stimulated Raman Spectroscopy. *Phys. Chem. Chem. Phys.* **2015**, *17*, 10454−10461.

(27) Ferrante, C.; Pontecorvo, E.; Cerullo, G.; Vos, M. H.; Scopigno, T. Direct Observation of Subpicosecond Vibrational Dynamics in Photoexcited Myoglobin. *Nat. Chem.* **2016**, *8*, 1137−1143.

(28) Leitner, D. M. Energy Flow in Proteins. *Annu. Rev. Phys. Chem.* **2008**, *59*, 233−259.

(29) Mukamel, S.; Biggs, J. D. Communication: Comment on the Effective Temporal and Spectral Resolution of Impulsive Stimulated Raman Signals. *J. Chem. Phys.* **2011**, *134*, 161101.

(30) Batignani, G.; Bossini, D.; Di Palo, N.; Ferrante, C.; Pontecorvo, E.; Cerullo, G.; Kimel, A.; Scopigno, T. Probing Ultrafast Photo-Induced Dynamics of the Exchange Energy in a Heisenberg Antiferromagnet. *Nat. Photonics* **2015**, *9*, 506−510.

(31) Fumero, G.; Batignani, G.; Dorfman, K. E.; Mukamel, S.; Scopigno, T. On the Resolution Limit of Femtosecond Stimulated Raman Spectroscopy: Modelling Fifth-Order Signals with Overlapping Pulses. *ChemPhysChem* **2015**, *16*, 3438−3443.

(32) Wende, T.; Liebel, M.; Schnedermann, C.; Pethick, R. J.; Kukura, P. Population-Controlled Impulsive Vibrational Spectroscopy: Background- and Baseline-Free Raman Spectroscopy of Excited Electronic States. *J. Phys. Chem. A* **2014**, *118*, 9976−9984.

(33) Kozma, I. Z.; Krok, P.; Riedle, E. Direct Measurement of the Group-Velocity Mismatch and Derivation of the Refractive-Index Dispersion for a Variety of Solvents in the Ultraviolet. *J. Opt. Soc. Am. B* **2005**, *22*, 1479−1485.

(34) Harris, F. On the Use of Windows for Harmonic Analysis with the Discrete Fourier Transform. *Proc. IEEE* **1978**, *66*, 51−83.